DTU Library

Efficient low-reflection fully etched vertical free-space grating couplers for suspended silicon photonics

Hansen, Søren Engelberth; Arregui, Guillermo; Babar, Ali Nawaz; Albrechtsen, Marcus; Lahijani, Babak Vosoughi; Christiansen, Rasmus Ellebæk; Stobbe, Søren

Published in:
Optics Express

Link to article, DOI:
10.1364/OE.485356

Publication date:
2023

Document Version
Publisher's PDF, also known as Version of record

Link back to DTU Orbit

Citation (APA):
Hansen, S. E., Arregui, G., Babar, A. N., Albrechtsen, M., Lahijani, B. V., Christiansen, R. E., & Stobbe, S. (2023). Efficient low-reflection fully etched vertical free-space grating couplers for suspended silicon photonics. *Optics Express*, *31*(11), 17424-17436. https://doi.org/10.1364/OE.485356

Research Article | Vol. 31, No. 11 / 22 May 2023 / Optics Express 17424

Optics EXPRESS

Efficient low-reflection fully etched vertical free-space grating couplers for suspended silicon photonics

SØREN ENGELBERTH HANSEN,[1,*] GUILLERMO ARREGUI,[1] ALI NAWAZ BABAR,[1,2] MARCUS ALBRECHTSEN,[1] BABAK VOSOUGHI LAHIJANI,[1] RASMUS ELLEBÆK CHRISTIANSEN,[2,3] AND SØREN STOBBE[1,2]

[1]*Department of Electrical and Photonics Engineering, Technical University of Denmark, Ørsteds Plads 345A, DK-2800 Kgs. Lyngby, Denmark*
[2]*NanoPhoton - Center for Nanophotonics, Technical University of Denmark, Ørsteds Plads 345A, DK-2800 Kgs. Lyngby, Denmark*
[3]*Department of Mechanical Engineering, Technical University of Denmark, Nils Koppels Alle 404, DK-2800 Kgs. Lyngby, Denmark*
[*]*senha@dtu.dk*

Abstract: We design and fabricate a grating coupler for interfacing suspended silicon photonic membranes with free-space optics while being compatible with single-step lithography and etching in 220 nm silicon device layers. The grating coupler design simultaneously and explicitly targets both high transmission into a silicon waveguide and low reflection back into the waveguide by means of a combination of a two-dimensional shape-optimization step followed by a three-dimensional parameterized extrusion. The designed coupler has a transmission of −6.6 dB (21.8 %), a 3 dB bandwidth of 75 nm, and a reflection of −27 dB (0.2 %). We experimentally validate the design by fabricating and optically characterizing a set of devices that allow the subtraction of all other sources of transmission losses as well as the inference of back-reflections from Fabry-Pérot fringes, and we measure a transmission of 19 % ± 2 %, a bandwidth of 65 nm and a reflection of 1.0 % ± 0.8 %.

1. Introduction

Suspended photonic structures in high-index dielectric slabs have recently shown great promise in new emerging devices such as photonic switches, interferometers, and filters [1–7]. Unlike conventional ridge waveguides and embedded waveguides, suspended structures are mechanically compliant, which enables the use of nano-opto-electro-mechanical components [8] for high-speed and low-power programmable photonics [4,9], hybrid quantum systems that can transduce signals between multiple domains [10,11], optomechanical sensors (mass, acceleration, magnetic fields, etc.) and integrated lasers in silicon [12]. In addition, the strong field confinement enabled by the air cladding enhances nonlinear effects [13,14]. Finally, suspended photonics enable integrated silicon photonics for mid-infrared applications, i.e., in the fingerprint region, as the platform allows low-loss operation compared to oxide claddings which absorb at these wavelengths [6,15,16].

In the quest to develop complex suspended nanophotonic circuitry, the accurate characterization of the scattering properties of passive and active photonic components is crucial. Such characterization typically involves testing of numerous nominally equivalent circuits, which in turn requires efficient, reproducible, and scalable ways to couple light into and out of the device. The coupling is typically achieved either by edge-coupling [17–19] or vertical coupling [20–40] and by employing either optical fibers in the near-field of the structure or free-space

#485356 https://doi.org/10.1364/OE.485356
Journal © 2023 Received 10 Jan 2023; revised 30 Mar 2023; accepted 27 Apr 2023; published 9 May 2023

Optics EXPRESS

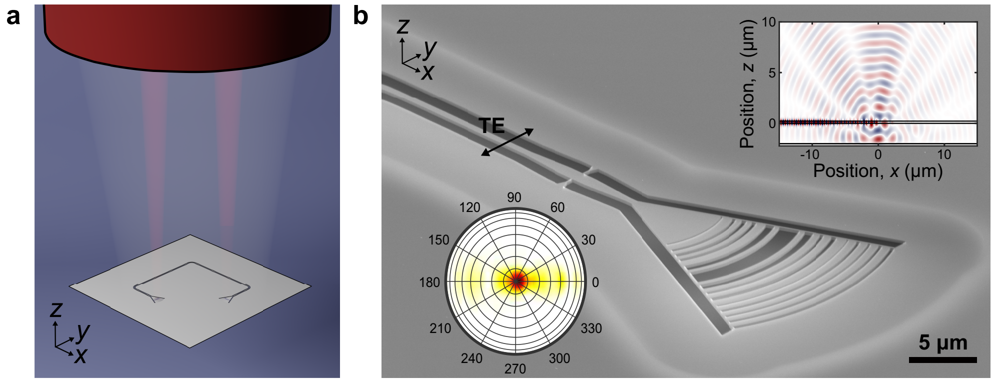

Fig. 1. Cross-polarized optical spectroscopy measurements using free-space grating couplers. a) Schematic of free-space coupling through a microscope objective in and out of a photonic chip. b) Scanning electron micrograph of the fabricated grating coupler along with the simulated far-field irradiance and the y-component of the electric field profile shown as insets. The polarization in the waveguides is transverse electric (TE) as indicated in the figure.

focusing optics. Edge-couplers generally consist of adiabatic waveguide expanders and, although they offer the best transmission over large bandwidths, they have difficult post-fabrication steps like cleaving and/or V-groove definition for accessing the waveguide ends and provide limited access-points to the circuits [41]. Vertical coupling offers great flexibility in the placement of input and output nodes, which makes them more practical for wafer-level testing and applications in research and industry. However, grating couplers use a diffractive grating to constructively scatter light propagating in a waveguide into the upward direction, making the designs highly dispersive. This sets limits on either the bandwidth or the transmission of the grating couplers [30]. For the past decade, extensive efforts have been devoted to bridging the gap between the performance of edge coupling and vertical coupling, leading to gratings with low insertion loss over bandwidths ranging from 30 to 140 nm [29,30]. Among those developments, fiber grating couplers that break the vertical symmetry to favor upwards over downwards scattering, such as shallow-etched gratings [23,24], multi-step gratings [25,26], blazed gratings [31,35], and mirror-backed gratings [24], have played a prominent role. Although fiber-based grating couplers dominate in applications due to their ease of integration into packaged devices [42], free-space grating couplers are essential for specific applications such as optical beam steering in LIDAR systems [43,44] or cryogenic experiments in quantum photonics [23], and they are highly beneficial for testing suspended photonic circuits. The absence of physical objects with large footprints, i.e., the optical fibers, in the near field of the structure, not only minimizes the risk of mechanical failure during testing and operation but allows also a more compact layout of the input and output nodes. Existing free-space grating couplers rarely consider back-reflections (in the remainder of this article referred to as reflections), although reflections are detrimental to the performance of photonic devices such as switches, interferometers, and filters. The conventional solution to suppress reflections is to couple in and out with a small tilt angle [23,24,32,33]. While effective, this approach complicates alignment compared to normal-incidence scattering. If one seeks a tilt-angle-free solution, the design of fully vertical grating couplers calls for explicitly including reflection minimization in the optimization scheme [25,26,34,35].

Here we present a suspended silicon free-space grating coupler designed for the C-band telecom wavelength window around 1550 nm, all-vertical coupling, low reflection, and transverse-electric light polarization that can be fabricated in a single etch step (Fig. 1). The free-space coupling from a microscope objective is illustrated in Fig. 1(a) and a scanning electron micrograph (SEM) of a characteristic fabricated device is shown in Fig. 1(b) along with the near-field of the electric field and the far-field irradiance, which shows that the scattering is vertical. Compared to other high-performance fiber and free-space grating couplers in the literature (see Table 1), our proposed device achieves reflections nearly as low as the best fiber grating couplers, a sufficient 3 dB bandwidth for most tunable light sources and super-luminescent diodes and a transmission comparable with previous grating couplers with similar characteristics, e.g., [20,21].

Table 1. Comparison of the present work with previously published grating couplers for transverse-electric modes. The grating couplers are listed by material, coupling scheme, tilt angle, waveguide type, and fabrication complexity quantified by the number of etch steps required for patterning. We compare the different designs by the performance of maximum transmission, T_{max}, the 3 dB bandwidth (BW), and the minimum reflection, R_{min}. The values are listed for simulated (S) and/or measured (M) grating coupler design.

Material	Coupling	Angle (°)	Type	Steps	T_{max} (dB)	3 dB BW (nm)	R_{min} (dB)	Ref.
Si	free-space	0	suspended	1	−6.6 (S) −7.1 (M)	75 (S) 65 (M)	−27 (S) −20 (M)	This work
Si_3N_4	free-space	0	suspended	1	−5 (S)	>200 (S)	-	[20]
diamond	free-space	0	suspended	1	−5.8 (M)	>90 (M)	-	[21]
Si	free-space	11	suspended	1	−6.6 (M)	15 (M)	<−7 (M)	[22]
GaAs	free-space	10	suspended	2	−2.2 (M)	40 (M)	<−20 (M)	[23]
Si_3N_4	free-space	13	suspended	2	−2.75 (M)	>200 (M)	-	[24]
Si	fiber	0	ridge	2	−1.0 (S)	>40 (S)	−21 (S)	[25]
Si & Si_3N_4	fiber	0	ridge	3	−0.57 (S)	>40 (S)	−31 (S)	[25]
Si	fiber	0	embedded	2	−0.6 (S) −1.5 (M)	69 (S) 49 (M)	−24 (S) −12 (M)	[26]
Si	fiber	10	suspended	1	−5.7 (M)	90 (M)	-	[27]
Si	fiber	10	ridge	1	−1.7 (M)	60 (M)	-	[28]
Si	fiber	25	ridge	1	−6 (M)	>140 (M)	−24 (M)	[29]

2. Design and optimization of the grating coupler

We design our grating coupler for coupling light focused by a microscope objective into a silicon waveguide of thickness t_{dev} = 220 nm and width of W = 500 nm that is suspended H_{box} = 2 µm above a silicon substrate. The simulations and optimization are run with a commercial finite-difference time-domain software (Lumerical 2021 R2.5) and the associated gradient-based optimizer (LumOpt-Python API). Due to the steep computational requirements of full three-dimensional numerical simulations, we employ a combination of a 2D adjoint gradient-based size optimization [45] in the xz-plane (The coordinate system is indicated in Fig. 1(b)) followed by an extrusion to 3D using a parametric optimization of a tapered focusing geometry. The geometry of the 2D optimization, including the input laser beam, is shown in Fig. 2(a) with the designable grating parameters, $g_1, g_2, \ldots, g_N$ indicating the width of the silicon and air stripes. The grating profile is optimized to simultaneously maximize the transmission from a converging free-space Gaussian beam with a beam-waist of 3.0 µm (based on spot-size measurement made on our optical setup using the knife-edge method [46]) into the silicon slab as well as to minimize reflections from the grating coupler into the silicon slab in the reverse configuration. The modeling is therefore implemented as two separate and independent finite-difference time-domain simulations.

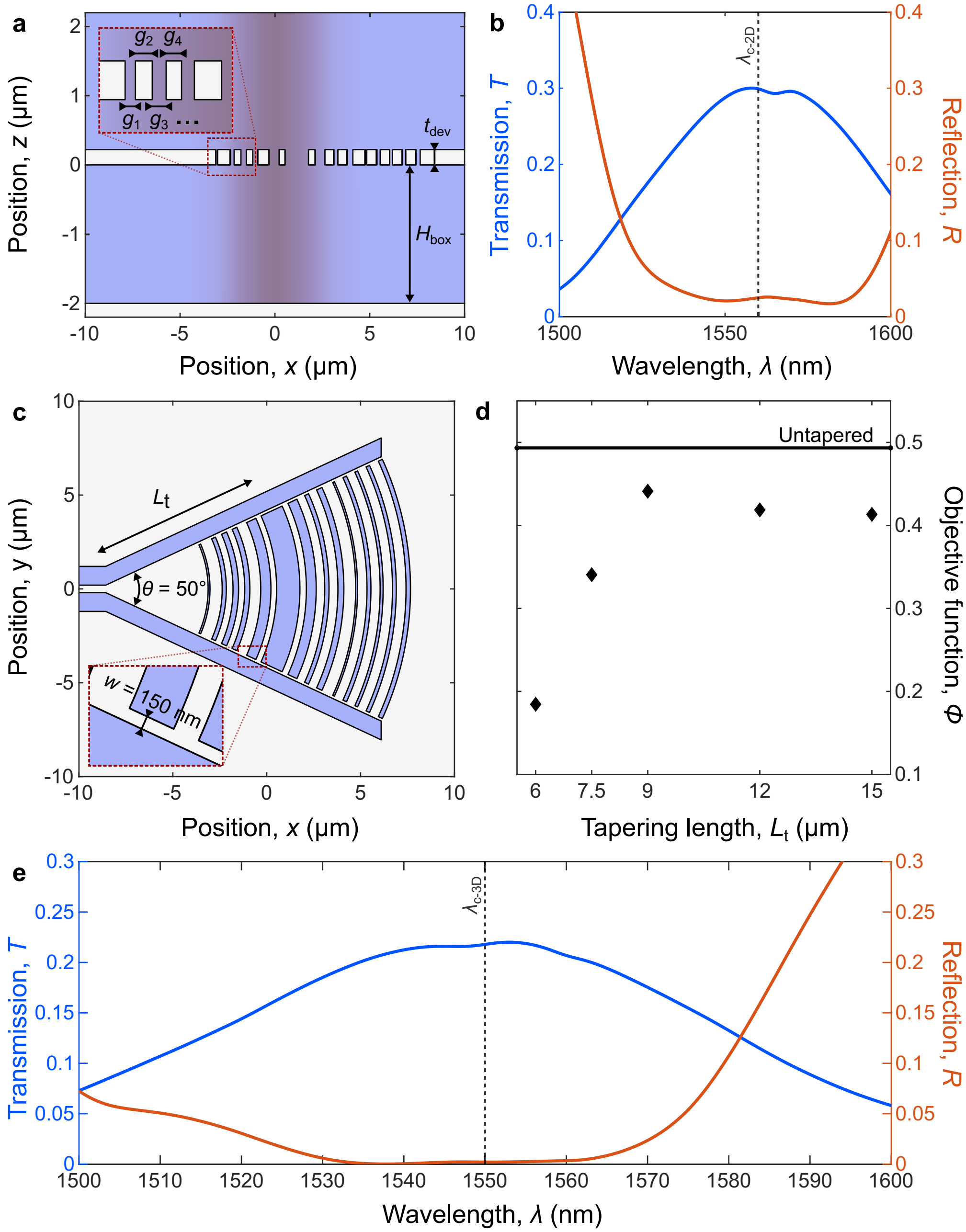

Fig. 2. Numerical design optimization of the grating coupler. (a) Side-view of grating geometry relative to the converging optical beam with the designable grating parameters, $g_1, g_2, \ldots, g_N$ illustrated in the inset. (b) Transmission and reflection of the 2D optimized grating. (c) Top-view of the tapered grating. (d) The performance of the focusing grating coupler compared with an untapered line grating with a width of 12 μm. (e) The transmission and reflection of the final 3D design with tapering length of 9 μm.

The objective function used is given by

$$\Phi = 2T_{\lambda_c} + \overline{T}_{100\ \mathrm{nm}} - 20\overline{R}_{50\ \mathrm{nm}}, \tag{1}$$

which corresponds to a weighted sum between the transmission at the target central wavelength, T_{λ_c}, the average transmission over a span of 100 nm, $\overline{T}_{100\ \mathrm{nm}}$, and the average reflection over a span of 50 nm around the central wavelength, $\overline{R}_{50\ \mathrm{nm}}$. The weighting is chosen to stress that the reflections should be small in the region near the central wavelength and to encourage the highest transmission at the targeted central wavelength. The target central wavelength is 1550 nm but is offset by +10 nm in the 2D optimization to account for a blue-shift that occurs upon extrusion of the geometry to 3D, partly due to the different effective mode refractive indices, and, more importantly, due to the difference between the beam shape in 2D (an infinitely extended trapezoid) and in 3D (a cone). The resulting grating profile and performance in 2D is shown in Figs. 2(a) and (b). The physical interpretation of the shape is as follows: The narrow trenches near the entrance to the waveguide serve as an anti-reflection structure for back-scattered light into the waveguide but are small enough not to scatter out-of-plane. In the region where the optical beam impinges onto the grating, the void features are wider in order to change the direction of propagation into the orthogonal direction. Similar shapes are commonly found for apodized gratings [23,28]. The 2D grating achieves a peak transmission of 30.0 % and a low reflection across the 3 dB bandwidth of the coupling.

When adapting the result from 2D to 3D, it is important to note that the end goal is to couple to the mode of a 500 nm wide waveguide rather than into an infinitely extruded silicon slab, which the 2D model does by construction. While the straightforward design choice would be to realize the coupler as a sufficiently wide rectangular grating followed by an adiabatic taper, this has been found in previous approaches to require excessively long tapering regions [47,48]. We use instead a design with curved grating lines that simultaneously couples the light beam in and reduces its width [33] (see Fig. 2(c)). The taper is surrounded, as does the silicon waveguide, by a 1 µm wide trench. The tapering angle is set to $\theta = 50°$, the width of the supporting beams to $w = 150$ nm and the tapering length from the optical beam center of the 2D optimized grating to the silicon strip waveguide, L_t, is swept to find the best performance as specified by the objective function, Φ, in Eq. (1). We observe that the highest performance is not obtained by making a longer taper, but with a tapering length of 9 µm as shown in Fig. 2(d), leading to a bounding-box footprint of $17{\times}16\,\mu\mathrm{m}^2$. For reference, we include in Fig. 2(d) the value obtained from an untapered 12 µm square-footprint grating coupler into a silicon waveguide of equal width. The local optimum emerges from the fixed choice of tapering angle, which determines a length that sets the suitable grating width for the spot size of the input beam. The grating parameters from the tapered design are listed in Table 2.

The dispersion of the transmission and the reflection of the final design are shown in Fig. 2(e). The final design exhibits a transmission and reflection at 1550 nm of −6.6 dB (21.8 %) and −27 dB (0.2 %) respectively, while the 3 dB-bandwidth is 75 nm. Compared to the 2D simulation, the center blue-shifts and the reflection decreases due to the aforementioned change in the shape of the mode. The transmission of −6.6 dB stems in part from the directionality, i.e., the fraction of light scattered upwards (−2.5 dB = 56 %), whereas the rest stems from the overlap with the vertical Gaussian mode in the far-field (see Fig. 1(b)). We note that the directionality could be improved further with approaches such as by introducing additional shallow etching steps, optimizing the thickness of the buried oxide layer, adding metallic mirrors, among others. However, we deliberately limit the design space to singly etched suspended structures made from the most standard SOI wafers, which feature a 220 nm device layer and a 2 µm buried oxide layer, in order to ensure direct process compatibility with the widest possible range of nanophotonics experiments that utilize the suspended platform.

Optics EXPRESS

Table 2. The grating parameters for the designed coupler. The grating is represented by the inner radii and width of the etch lines to simplify creating masks for fabrication, of which the width corresponds to the odd design parameters, $g_1, g_3, g_5, \ldots$, and the even design parameters take part in the position of the start of the etch lines. The tapering angle is $\theta = 50°$.

Grating line no.	Inner radius (nm)	Width (nm)	Grating line no.	Inner radius (nm)	Width (nm)
1	5879	100	8	12090	230
2	6629	219	9	12794	316
3	7206	296	10	13740	101
4	7830	272	11	14342	209
5	8682	542	12	15042	159
6	9528	1240	13	15700	201
7	11111	525	14	16422	236

3. Experimental characterization

We fabricate the grating coupler from silicon-on-insulator wafers with a t_{dev} = 220 nm device layer and a H_{box} = 2 µm buried oxide layer. The pattern is written, along with silicon waveguides and other components, by a single step of electron-beam lithography, transferred into silicon by reactive ion etching and made into a suspended structure by a vapor HF underetch [49,50]. The grating couplers are characterized by performing transmission measurements on suspended silicon circuits that use both the designed coupler for in- and out-coupling. In order to account for propagation losses in the waveguide, we use a series of circuits with different total waveguide lengths varying from $L = 0.25$ mm to 3.25 mm and employ the cut-back method to extract the loss [51]. An example of such a set of circuits is shown in the dark-field microscope image of Fig. 3(a). The grating couplers are placed orthogonally to each other and at a center-to-center distance of 71 µm, which allows the use of spatial and polarization-resolved measurements through a cross-polarized microscopy setup. A representative SEM of a fabricated grating coupler is shown in Fig. 3(b).

Figure 3(c) shows the dispersion of the transmitted power measured for a set of circuits of varying lengths. The data is normalized to a reference measurement on a gold mirror and therefore only includes loss associated with coupling loss of the grating couplers and propagation loss through the circuit. We extract the propagation losses by linear fits of the log-scale transmission as a function of waveguide length after smoothing out the observed fringes by a moving average of 1.5 nm followed by a Gaussian convolution with full-width-half-maximum of 5 nm. This smoothing procedure is chosen because we find that it precisely recovers the correct coupler transmission when applied to the transmitted power generated by a transfer-matrix Fabry-Pérot model of two reflective couplers regardless of their reflectivity (the model is discussed in further detail below). The fits shown in Fig. 3(d) are performed on a data set that includes measurements on eight sets of cut-back circuits: two nominally identical sets for each of four sets with grating couplers that in the lithographic mask are subject to four different fixed growths of the width of the void grating lines, δ, relative to the designed parameters. More details on δ are provided below. We independently extract the propagation loss for circuits with different δ and take their average to extract the propagation loss for our suspended silicon waveguides, whose geometry is common to all circuits regardless of δ. We extract a suspended waveguide loss of 1.32 dB/mm ± 0.05 dB/mm; a value that includes both extrinsic losses from sidewall roughness and the losses associated with the tethers supporting the suspended waveguide. The transmission of the grating coupler is found by taking the square root of the transmitted power in each circuit after correction for the propagation loss, which assumes identical performance of the input and output grating

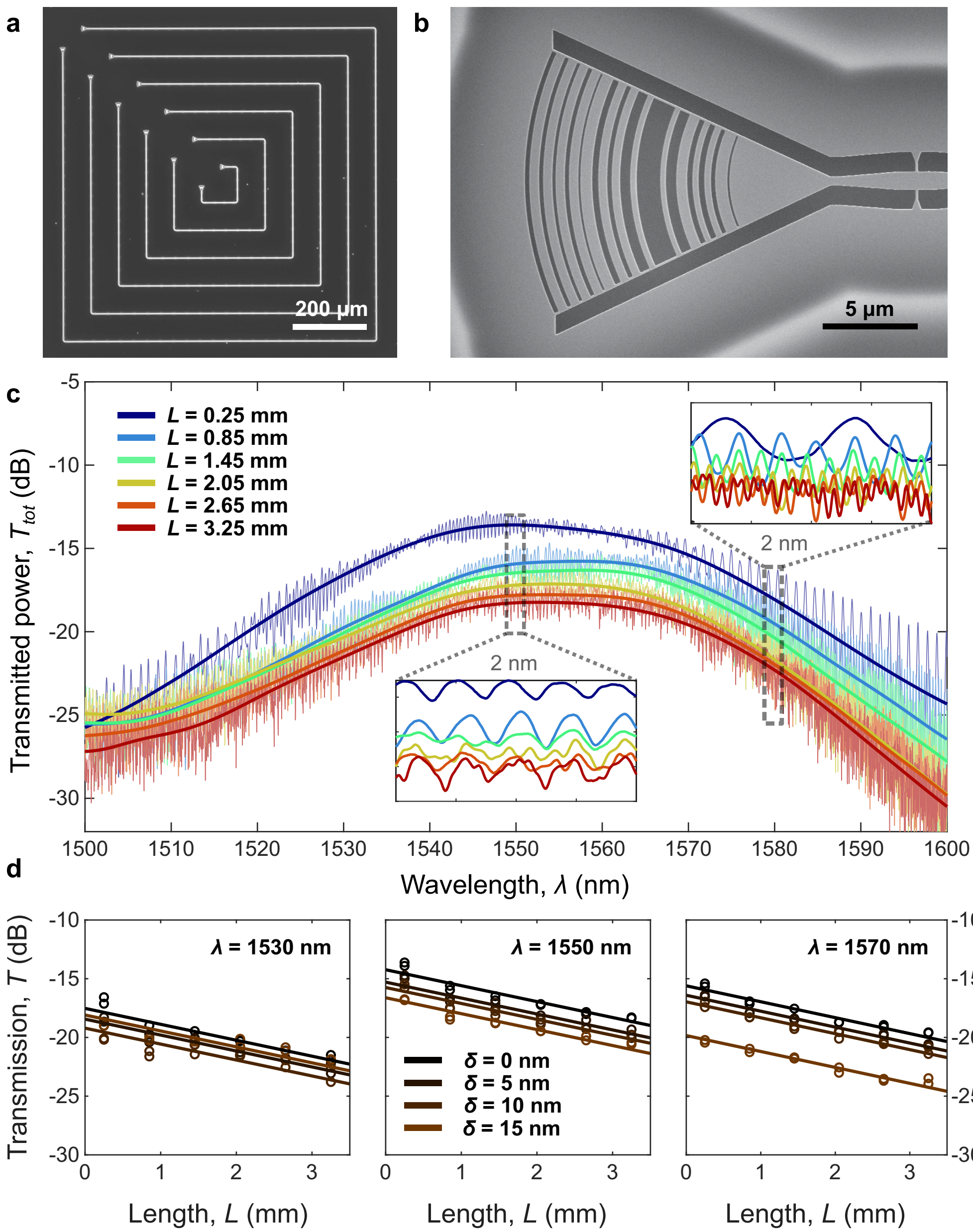

Fig. 3. Experimental characterization of grating couplers. a) Dark-field optical micrograph of a set of waveguide circuits with lengths varying between 0.25 mm and 3.25 mm. b) Top-view scanning electron micrograph of a fabricated grating coupler. c) Raw data from transmission measurements of circuits with different lengths. The mean transmitted power shows the circuit-to-circuit transmission, while the reflection amounts to the various oscillations shown in the insets of 2 nm wide wavelength windows at 1550 nm and 1580 nm. d) Linear fits of the propagation loss for different linewidth reductions, δ, (see Fig. 6(a)) of grating couplers displayed at three wavelengths, $\lambda \in \{1530\text{ nm}, 1550\text{ nm}, 1570\text{ nm}\}$.

Optics EXPRESS

couplers, following a recursive procedure as detailed in Supplement 1 and discussed further below.

We extract the reflection from the grating coupler back into the silicon waveguide by analyzing the observed fringes in the raw data around the smoothed transmission data. Reflections at both grating couplers generate Fabry-Pérot fringes with a free spectral range (FSR) that is inversely proportional to the circuit length and whose amplitude scales with the reflectance [52]. However, as seen in the two insets of Fig. 3(c), the oscillations dominating at the central wavelengths are identical in period for different lengths and thus do not originate from such Fabry-Pérot resonances. We find that the fringes with FSR of 0.4 nm correspond to vertical back-reflections from the 775 µm silicon substrate that induce oscillations in the transmission through the devices. They originate due to the polished back-surface of the employed SOI wafers and could easily be reduced by simply choosing single-polished SOI wafers. To extract the reflection of the grating coupler and compare it to the simulations in Fig. 2 that do not include the full silicon handle layer, we perform a windowed Fourier transform of the transmitted power and analyze the FSR of the oscillations and their amplitudes in small wavelength windows of 10 nm at a time.

The transformation illustrates the presence of two sets of peaks as shown in Fig. 4: One varying with circuit length and one that remains fixed. The former is associated with in-plane circuit reflections, while the latter corresponds to vertical substrate reflections. The amplitude of the circuit reflections varies strongly through the grating coupler bandwidth, indicating a strongly

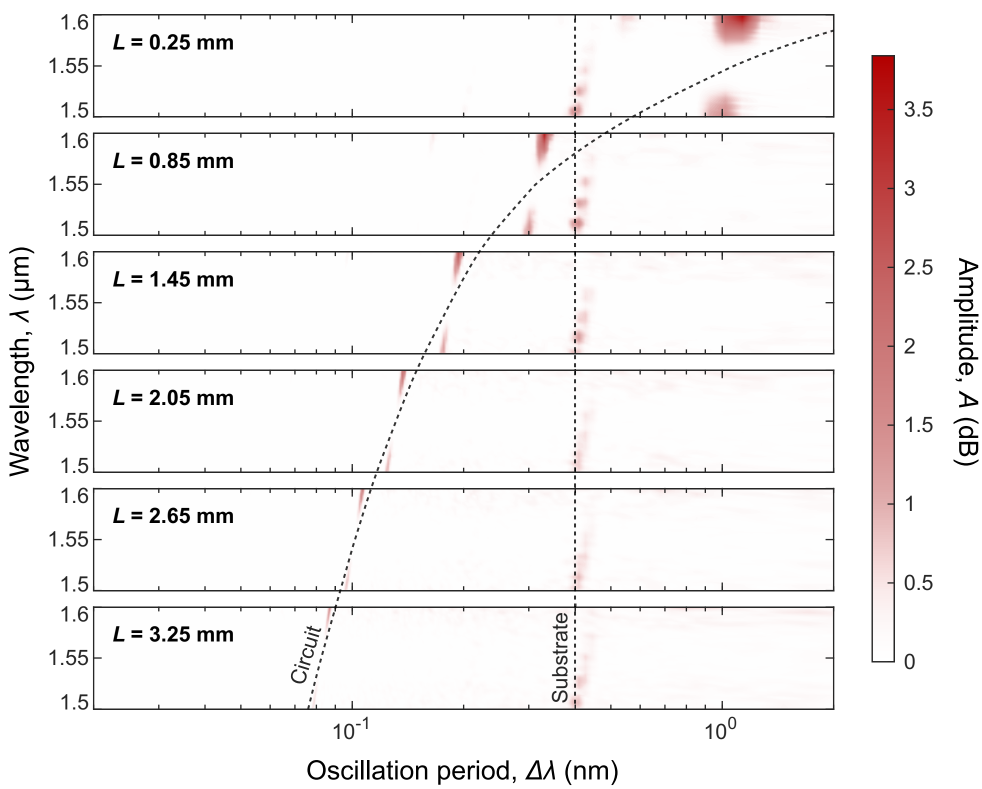

Fig. 4. Windowed Fourier spectra of oscillation amplitudes in the transmitted power. The spectra for varying lengths from 0.25 mm to 3.25 mm show the distinction between amplitudes that are fixed in oscillation period and those that are length-dependent and related to the reflections from the grating couplers as highlighted with the dashed curves.

dispersive reflectance. We model the total circuit transmission, $T_{\mathrm{tot}}(\lambda)$, based on the transmission, $T(\lambda)$, and reflection, $R(\lambda)$, of the grating coupler

$$T_{\mathrm{tot}}(\lambda) = \frac{T^2(\lambda)\,\mathrm{e}^{-\alpha L}}{|1 - R(\lambda)\,\mathrm{e}^{i2\beta(\lambda)L}\mathrm{e}^{-\alpha L}|} \tag{2}$$

where $\alpha/2$ and β are the real and imaginary part of the propagation constant. The model is generalized from Ref. [23] to include propagation losses and assumes identical grating couplers. A Taylor expansion to fourth order of the denominator with respect to R (see Supplement 1 for more information) shows that the amplitude of the oscillations in the transmitted power (i.e., not to be confused with the amplitude of the electric field) for the first round-trip reflection, $A_1(\lambda)$, is given by

$$A_1(\lambda) \approx 2\mathrm{e}^{-2\alpha L}(R(\lambda) + \mathrm{e}^{-2\alpha L}R^3(\lambda))T^2(\lambda) \tag{3}$$

We find the polynomial roots of the reflection from the circuit peaks (Fig. 4) and obtain the reflection curves for each circuit.

The mean measured transmission and reflection are shown in Fig. 5, with the error bar showing two times the standard deviation extracted from the 12 circuits used. We obtain a good qualitative agreement between the measured and the designed characteristics of the grating coupler. However, the reflection is larger in the measurement at the edges of the coupling bandwidth, which we attribute to minor deviations between the design and the fabricated geometries. These deviations are primarily of three types: a fixed or average growth/shrinking of the etched voids due to the entire fabrication process, line-to-line local variations of such growth due to aspect-ratio dependent etching, and sidewall and line-edge roughness [53]. We investigate the impact of such deviations by simulating the grating coupler with the geometric parameters of the fabricated device,

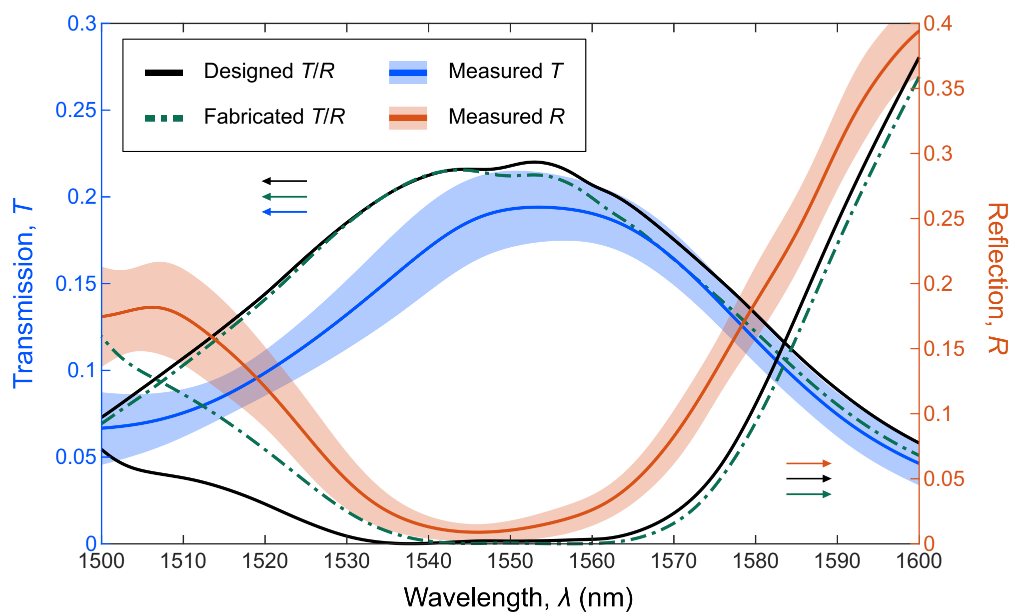

Fig. 5. Comparison of transmission and reflection for the simulated and experimentally evaluated grating coupler. The wavelength-dependent experimental transmission (left y-axis) and reflection (right y-axis) of the grating coupler are represented by the extracted mean (solid line) and the standard error (shaded region of 2 times the standard deviation). The simulated curves for the optimized design (solid black lines) and the fabricated structure (dashed green lines) are also included.

Optics EXPRESS

the approximated geometry of which is obtained from high-magnification and high-resolution SEM image analysis. The pixel-to-nanometer conversion is performed by calibrating with a uniform 50 % duty cycle and 400 nm period grating. The simulated transmission and reflection for the fabricated grating coupler are also shown in Fig. 5. We observe that design-to-fabrication deviations explain the increased reflection at short wavelengths but do not capture neither the

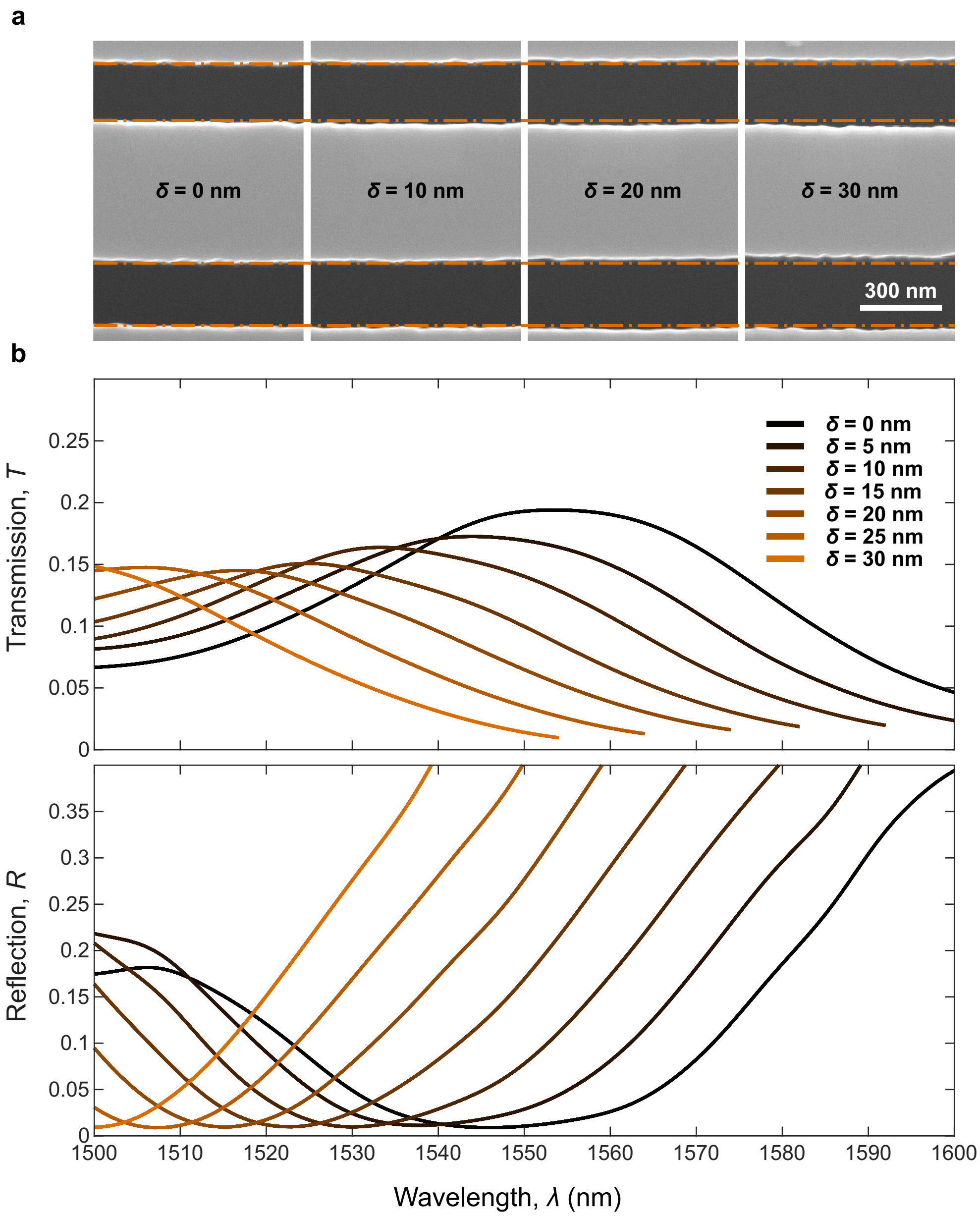

Fig. 6. Tolerance against fabrication imperfections in the form of linewidth reductions. a) Top-view scanning electron micrographs of grating lines with different linewidth reductions, δ. The dashed orange lines show the linewidth reduction compared to the target width. b) The mean measured transmission (top) and reflection (bottom) for grating couplers with different values of δ.

drop in transmission in the same range nor the higher reflection at long wavelengths. While lower transmission may follow from positional misalignment, we attribute the remaining discrepancy in the shape of the reflection and transmission curves to sidewall and line-edge roughness, which are not taken into account in the simulation of the fabricated device.

Finally, we investigate the versatility of the proposed design for use at other central wavelengths. This is achieved by repeating the full experimental characterization for grating couplers with different δ. The effect of δ on the fabricated geometries is shown in the SEMs of Fig. 6(a). The decreased effective index induced by the larger air filling leads to a monotonic blue-shift as shown in the measured transmission and reflection curves in Fig. 6(b). In addition, we observe only minor degradation of the grating-coupler characteristics with more linewidth reduction. We find from a linear fit that the maximum transmission only decreases by $\mathrm{d}T_{\max}/\mathrm{d}\delta = -0.2\%/\mathrm{nm}$. The tunability of the center wavelength shows that the design can be readily adjusted for testing applications that require different central wavelengths before commencing a new design optimization.

4. Conclusion

In summary, we design and experimentally validate a new grating coupler that enables a robust, efficient and undemanding testing of and interfacing with suspended silicon membrane circuits. The grating coupler operates by coupling vertically into free-space, which facilitates easy device testing with microscope setups. Furthermore, the grating consists of lines fully etched through the silicon device layer, which allows fabrication of suspended devices, such as nano-electro-mechanical devices, waveguide-coupled photonic cavities, and optomechanical devices, in a single lithography step. The designed grating coupler shows a simulated transmission and reflection of 21.8 % and 0.2 % at the central wavelength 1550 nm along with a 3 dB bandwidth of 75 nm. A thorough analysis of the transmission and reflection has been undertaken, which demonstrates the transmission of 19 % ± 2 % and the reflection of 1.0 % ± 0.8 %.

Funding. Innovationsfonden (0175-00022, 2054-00008); Danmarks Grundforskningsfond (DNRF147); Danmarks Frie Forskningsfond (0135-00315); European Research Council (101045396); HORIZON EUROPE European Research Council (101067606).

Acknowledgments. We thank Thor August Schimmell Weis, Konstantinos Tsoukalas, and Christian Anker Rosiek for valuable discussions on the experiment.

Disclosures. The authors declare no conflicts of interest.

Data availability. The data underlying the results presented in this paper are not publicly available at this time but may be obtained from the authors upon reasonable request.

Supplemental document. See Supplement 1 for supporting content.

References

1. T. H. Stievater, M. W. Pruessner, W. S. Rabinovich, D. Park, R. Mahon, D. A. Kozak, J. B. Boos, S. A. Holmstrom, and J. B. Khurgin, "Suspended photonic waveguide devices," Appl. Opt. **54**(31), F164–F173 (2015).
2. K. Takahashi, Y. Kanamori, Y. Kokubun, and K. Hane, "A wavelength-selective add-drop switch using silicon microring resonator with a submicron-comb electrostatic actuator," Opt. Express **16**(19), 14421–14428 (2008).
3. M. Albrechtsen, B. Vosoughi Lahijani, R. E. Christiansen, V. T. H. Nguyen, L. N. Casses, S. E. Hansen, N. Stenger, O. Sigmund, H. Jansen, J. Mørk, and S. Stobbe, "Nanometer-scale photon confinement in topology-optimized dielectric cavities," Nat. Commun. **13**(1), 6281 (2022).
4. H. Du, F. S. Chau, and G. Zhou, "Mechanically-tunable photonic devices with on-chip integrated mems/nems actuators," Micromachines **7**(4), 69 (2016).
5. H. Cai, B. Dong, J. F. Tao, L. Ding, J. M. Tsai, G. Q. Lo, A. Q. Liu, and D. L. Kwong, "A nanoelectromechanical systems optical switch driven by optical gradient force," Appl. Phys. Lett. **102**(2), 023103 (2013).
6. R. S. El Shamy, M. A. Swillam, and D. A. Khalil, "Mid infrared integrated mzi gas sensor using suspended silicon waveguide," J. Lightwave Technol. **37**(17), 4394–4400 (2019).
7. M. Li, W. H. Pernice, and H. X. Tang, "Ultrahigh-frequency nano-optomechanical resonators in slot waveguide ring cavities," Appl. Phys. Lett. **97**(18), 183110 (2010).

8. L. Midolo, A. Schliesser, and A. Fiore, "Nano-opto-electro-mechanical systems," Nat. Nanotechnol. **13**(1), 11–18 (2018).
9. W. Bogaerts, D. Pérez, J. Capmany, D. A. Miller, J. Poon, D. Englund, F. Morichetti, and A. Melloni, "Programmable photonic circuits," Nature **586**(7828), 207–216 (2020).
10. H. Ren, M. H. Matheny, G. S. MacCabe, J. Luo, H. Pfeifer, M. Mirhosseini, and O. Painter, "Two-dimensional optomechanical crystal cavity with high quantum cooperativity," Nat. Commun. **11**(1), 3373 (2020).
11. A. N. Cleland and M. R. Geller, "Superconducting qubit storage and entanglement with nanomechanical resonators," Phys. Rev. Lett. **93**(7), 070501 (2004).
12. N. T. Otterstrom, R. O. Behunin, E. A. Kittlaus, Z. Wang, and P. T. Rakich, "A silicon brillouin laser," Science **360**(6393), 1113–1116 (2018).
13. H. Cong, B. Yang, W. Wei, J. Wang, Q. Feng, Z. Wang, T. Wang, X. Guo, and J. Zhang, "Suspended algaas waveguide for integrated nonlinear photonics," Appl. Phys. Lett. **119**(13), 133502 (2021).
14. Y. Zhang, Z. Cheng, L. Liu, B. Zhu, J. Wang, W. Zhou, X. Wu, and H. K. Tsang, "Enhancement of self-phase modulation induced spectral broadening in silicon suspended membrane waveguides," J. Opt. **18**(5), 055503 (2016).
15. J. Soler Penadés, C. Alonso-Ramos, A. Z. Khokhar, M. Nedeljkovic, L. A. Boodhoo, A. Ortega-Mo nux, I. Molina-Fernández, P. Cheben, and G. Z. Mashanovich, "Suspended soi waveguide with sub-wavelength grating cladding for mid-infrared," Opt. Lett. **39**(19), 5661–5664 (2014).
16. Z. Cheng, X. Chen, C. Y. Wong, K. Xu, C. K. Fung, Y. M. Chen, and H. K. Tsang, "Focusing subwavelength grating coupler for mid-infrared suspended membrane waveguide," Opt. Lett. **37**(7), 1217–1219 (2012).
17. S. Wang, Q. Wang, J. Wang, Z. Tu, W. Wang, L. Jia, M. Yu, Q. Fang, and Y. Cai, "High-efficiency suspended three-tip edge coupler for mid-infrared photonics," Opt. Commun. **488**, 126512 (2021).
18. Y. Xiao, Y. Xu, Y. Dong, B. Zhang, and Y. Ni, "A 60 um-long fiber-to-chip edge coupler assisted by subwavelength grating structure with ultralow loss and large bandwidth," Photonics **9**(6), 413 (2022).
19. L. Jia, C. Li, T. Y. Liow, and G. Q. Lo, "Efficient suspended coupler with loss less than -1.4 db between si-photonic waveguide and cleaved single mode fiber," J. Lightwave Technol. **36**(2), 239–244 (2018).
20. C. Barth, J. Wolters, A. W. Schell, J. Probst, M. Schoengen, B. Löchel, S. Kowarik, and O. Benson, "Miniaturized bragg-grating couplers for sin-photonic crystal slabs," Opt. Express **23**(8), 9803–9811 (2015).
21. C. Dory, D. Vercruysse, K. Y. Yang, N. V. Sapra, A. E. Rugar, S. Sun, D. M. Lukin, A. Y. Piggott, J. L. Zhang, M. Radulaski, K. G. Lagoudakis, L. Su, and J. Vuckovic, "Inverse-designed diamond photonics," Nat. Commun. **10**(1), 3309 (2019).
22. E. Schelew, G. W. Rieger, and J. F. Young, "Characterization of integrated planar photonic crystal circuits fabricated by a cmos foundry," J. Lightwave Technol. **31**(2), 239–248 (2013).
23. X. Zhou, I. Kulkova, T. Lund-Hansen, S. L. Hansen, P. Lodahl, and L. Midolo, "High-efficiency shallow-etched grating on gaas membranes for quantum photonic applications," Appl. Phys. Lett. **113**(25), 251103 (2018).
24. Y. Zhu, J. Wang, W. Xie, B. Tian, Y. Li, E. Brainis, Y. Jiao, and D. V. Thourhout, "Ultra-compact silicon nitride grating coupler for microscopy systems," Opt. Express **25**(26), 33297–33304 (2017).
25. S. Hooten, T. V. Vaerenbergh, P. Sun, S. Mathai, Z. Huang, and R. G. Beausoleil, "Adjoint optimization of efficient cmos-compatible si-sin vertical grating couplers for dwdm applications," J. Lightwave Technol. **38**(13), 3422–3430 (2020).
26. T. Watanabe, M. Ayata, U. Koch, Y. Fedoryshyn, and J. Leuthold, "Perpendicular grating coupler based on a blazed antiback-reflection structure," J. Lightwave Technol. **35**(21), 4663–4669 (2017).
27. Z. Cheng, X. Chen, C. Y. Wong, K. Xu, and H. K. Tsang, "Apodized focusing subwavelength grating couplers for suspended membrane waveguides," Appl. Phys. Lett. **101**(10), 101104 (2012).
28. Y. Ding, H. Ou, and C. Peucheret, "Ultrahigh-efficiency apodized grating coupler using fully etched photonic crystals," Opt. Lett. **38**(15), 2732–2734 (2013).
29. Y. Wang, W. Shi, X. Wang, Z. Lu, M. Caverley, R. Bojko, L. Chrostowski, and N. A. Jaeger, "Design of broadband subwavelength grating couplers with low back reflection," Opt. Lett. **40**(20), 4647–4650 (2015).
30. N. V. Sapra, D. Vercruysse, L. Su, K. Y. Yang, J. Skarda, A. Y. Piggott, and J. Vuckovic, "Inverse design and demonstration of broadband grating couplers," IEEE J. Sel. Top. Quantum Electron. **25**(3), 1–7 (2019).
31. B. Wang, J. Jiang, and G. P. Nordin, "Embedded slanted grating for vertical coupling between fibers and silicon-on-insulator planar waveguides," IEEE Photonics Technol. Lett. **17**(9), 1884–1886 (2005).
32. D. Taillaert, P. Bienstman, and R. Baets, "Compact efficient broadband grating coupler for silicon-on-insulator waveguides," Opt. Lett. **29**(23), 2749–2751 (2004).
33. F. Van Laere, G. Roelkens, M. Ayre, J. Schrauwen, D. Taillaert, D. Van Thourhout, T. F. Krauss, and R. Baets, "Compact and highly efficient grating couplers between optical fiber and nanophotonic waveguides," J. Lightwave Technol. **25**(1), 151–156 (2007).
34. A. Michaels and E. Yablonovitch, "Inverse design of near unity efficiency perfectly vertical grating couplers," Opt. Express **26**(4), 4766–4779 (2018).
35. L. Su, R. Trivedi, N. V. Sapra, A. Y. Piggott, D. Vercruysse, and J. Vuckovic, "Fully-automated optimization of grating couplers," Opt. Express **26**(4), 4023–4034 (2018).
36. A. Faraon, I. Fushman, D. Englund, N. Stoltz, P. Petroff, and J. Vuckovic, "Dipole induced transparency in waveguide coupled photonic crystal cavities," Opt. Express **16**(16), 12154–12162 (2008).

Optics EXPRESS

37. C. C. Tsai, J. Mower, and D. Englund, "Directional free-space coupling from photonic crystal waveguides," Opt. Express **19**(21), 20586–20596 (2011).
38. W. Zhou, Z. Cheng, X. Sun, and H. K. Tsang, "Tailorable dual-wavelength-band coupling in a transverse-electric-mode focusing subwavelength grating coupler," Opt. Lett. **43**(12), 2985–2988 (2018).
39. Z. Cheng, X. Chen, C. Y. Wong, K. Xu, and H. K. Tsang, "Broadband focusing grating couplers for suspended-membrane waveguides," Opt. Lett. **37**(24), 5181–5183 (2012).
40. J. Kang, Z. Cheng, W. Zhou, T. H. Xiao, K. L. Gopalakrisna, M. Takenaka, H. K. Tsang, and K. Goda, "Focusing subwavelength grating coupler for mid-infrared suspended membrane germanium waveguides," Opt. Lett. **42**(11), 2094–2097 (2017).
41. R. Marchetti, C. Lacava, L. Carroll, K. Gradkowski, and P. Minzioni, "Coupling strategies for silicon photonics integrated chips," Photonics Res. **7**(2), 201–239 (2019).
42. L. Carroll, J. S. Lee, C. Scarcella, K. Gradkowski, M. Duperron, H. Lu, Y. Zhao, C. Eason, P. Morrissey, M. Rensing, S. Collins, H. Y. Hwang, and P. O'Brien, "Photonic packaging: Transforming silicon photonic integrated circuits into photonic devices," Appl. Sci. **6**(12), 426 (2016).
43. C. Errando-Herranz, N. Le Thomas, and K. B. Gylfason, "Low-power optical beam steering by microelectromechanical waveguide gratings," Opt. Lett. **44**(4), 855–858 (2019).
44. Y. C. Chang, M. C. Shin, C. T. Phare, S. A. Miller, E. Shim, and M. Lipson, "2d beam steerer based on metalens on silicon photonics," Opt. Express **29**(2), 854–864 (2021).
45. C. M. Lalau-Keraly, S. Bhargava, O. D. Miller, and E. Yablonovitch, "Adjoint shape optimization applied to electromagnetic design," Opt. Express **21**(18), 21693–21701 (2013).
46. A. H. Firester, M. E. Heller, and P. Sheng, "Knife-edge scanning measurements of subwavelength focused light beams," Appl. Opt. **16**(7), 1971–1974 (1977).
47. Y. Fu, T. Ye, W. Tang, and T. Chu, "Efficient adiabatic silicon-on-insulator waveguide taper," Photonics Res. **2**(3), A41–A44 (2014).
48. D. Taillaert, F. Van Laere, M. Ayre, W. Bogaerts, D. Van Thourhout, P. Bienstman, and R. Baets, "Grating couplers for coupling between optical fibers and nanophotonic waveguides," Jpn. J. Appl. Phys. **45**(8A), 6071–6077 (2006).
49. C. A. Rosiek, G. Arregui, A. Vladimirova, M. Albrechtsen, B. V. Lahijani, R. E. Christiansen, and S. Stobbe, "Observation of strong backscattering in valley-hall photonic topological interface modes," Nat. Photon., **17**, 386 (2022).
50. G. Arregui, R. C. Ng, M. Albrechtsen, S. Stobbe, C. M. Sotomayor-Torres, and P. D. García, "Cavity optomechanics with anderson-localized optical modes," Phys. Rev. Lett. **130**(4), 043802 (2023).
51. Y. A. Vlasov and S. J. McNab, "Losses in single-mode silicon-on-insulator strip waveguides and bends," Opt. Express **12**(8), 1622–1631 (2004).
52. N. Ismail, C. C. Kores, D. Geskus, and M. Pollnau, "Fabry-pérot resonator: Spectral line shapes, generic and related airy distributions, linewidths, finesses, and performance at low or frequency-dependent reflectivity," Opt. Express **24**(15), 16366–16389 (2016).
53. R. A. Gottscho, C. W. Jurgensen, and D. J. Vitkavage, "Microscopic uniformity in plasma etching," J. Vac. Sci. Technol., B: Microelectron. Process. Phenom. **10**(5), 2133–2147 (1992).